Modern Physics Letters B
Vol. 34, No. 14 (2020) 2050145 (18 pages)

DOI: 10.1142/S0217984920501456

Investigation of turbulence-induced quadrupole source acoustic characteristics of a three-dimensional hydrofoil

Rennian Li*, Wenna Liang†, Wei Han‡, Hui Quan§, Rong Guo¶ and Pi Long Tian‖

College of Energy and Power Engineering, Lanzhou University of Technology, Lanzhou, Gansu Province 730050, China
Key Laboratory of Fluid Machinery and Systems, Lanzhou, Gansu Province 730050, China
*lirn@lut.cn
†wennaliang948210@163.com
‡hanwei@lut.cn
§quanh2010@163.com
¶xizhilang@163.com
‖13383498877@163.com

Guoyi Peng

College of Engineering, Nihon University, Koriyama, Fukushima 963-8642, Japan
peng@mech.ce.nihon-u.ac.jp

Received 27 August 2019
Revised 25 October 2019
Accepted 25 November 2019
Published 14 May 2020

In order to investigate the turbulence-induced acoustic characteristics of hydrofoils, the flow and sound field for a model NH-15-18-1 asymmetric hydrofoil were calculated based on the mixed method of large eddy simulation (LES) with Lighthill analogy theory. Unsteady fluid turbulent stress source around the hydrofoil were selected as the inducements of quadrupole sound. The average velocity along the mainstream direction was calculated for different Reynolds numbers (Re). Compared to experimental measurements, good agreement was seen over a range of Re. The results showed that the larger the Re, the larger the vortex intensity, the shorter the vortex initial shedding position to the leading edge of the hydrofoil, and the higher the vortex shedding frequency (f_s). The maximum sound pressure level (SPL) of the hydrofoil was located at the trailing edge and wake of the hydrofoil, which coincided with the velocity curl (ω) distribution of the flow field. The maximum SPL of the sound field was consistent with the location of the vortex shedding. There were quadratic positive correlations between the total sound pressure level (TSPL) and the maximum value of the vortex intensity ($\Gamma_{\max}$) and velocity curl, which verified that shedding and diffusion of vortices are the fundamental cause of the generation of the quadrupole source noise.

Keywords: Turbulent noise; quadrupole sound source; hydrofoil; Reynolds number; vortex.

†,‡Corresponding authors.

1. Introduction

As is well known, turbulence induced by the flow around an airfoil is a common phenomenon in fluid machinery, such as pumps, wind turbines, and hydraulic turbines.[1] Compared with an ordinary cascade, the airfoil structure is more complex, and its hydrodynamic characteristics also have different flow regimes due to the particularity of its own structure. The edge effect usually produces noise. Studying the airfoil noise can provide a theoretical basis for studying other complex rotating machinery. The acoustic source generated by the stress change of the turbulent fluid around the airfoil during the mechanical operation of the fluid can be regarded as the result of the interaction between the fluids. The source of sound generated by the interaction between fluids is defined as the turbulent stress source of fluid.[2]

Turbulence-induced noise has been investigated by many scholars in the world. Fan *et al.*[3] studied turbulence-induced two-dimensional hydrofoil vibration and noise characteristics. The results showed that the velocity and airfoil angle of attack had a significant impact on noise sound pressure level (SPL). Ai *et al.*[4] simulated the separation flow of an isolated airfoil under different Reynolds numbers (Re). It was noted that the large eddy simulation (LES) method had sufficient reliability and prediction accuracy for the simulation of the isolated airfoil separation flow. Long *et al.*[5] investigated the aerodynamics around the cylinder under different Re. Numerical simulation results of the noise showed that reducing the Re or frequency of vortex shedding on the cylindrical surface could reduce the influence of unsteady pulse dynamics, thus reducing the aerodynamic noise around the cylinder. There is disagreement in the literature around the degree of influence of quadrupole noise at low Mach numbers. The research in Refs. 6 and 7 shows that the effects of quadrupole are small in both low frequency and high frequency stages. Giret *et al.*[8] identified that quadrupole noise has a large impact on the low-frequency band and has a small effect on the high-frequency band. Boudet *et al.*[9] denoted that quadrupole noise has a small effect on the low-frequency band and has a large impact on the high-frequency band.

To sum up, at present, world-wide scholarly research on turbulence noise has mainly focused on the dipole source generated by pressure pulsation, ignoring the quadrupole sound source generated by turbulent stress. However, for underwater submarines, the mid–low-frequency noise induced by turbulence is one of the primary sources of noise. The noise penetration force has a wide transmission range and is therefore difficult to shield for stealth technology. In this paper, the model NH-15-18-1 asymmetric airfoil was selected as the object to study the turbulent noise of the hydrofoil with different Re based on the mixed method of LES with Lighthill analogy theory.

2. Mixed Method of LES with Lighthill Analogy Theory

2.1. *Flow field numerical calculation methods*

2.1.1. *Geometric model*

A three-dimensional model was based on the NH-15-18-1 hydrofoil, shown in Fig. 1. The hydrofoil chord (C) and thickness were 100 mm and 30 mm, respectively. The front half of flow region was semicircular, with a radius of 300 mm, and the rear half was rectangular, with a length of 500 mm and a width of 600 mm.

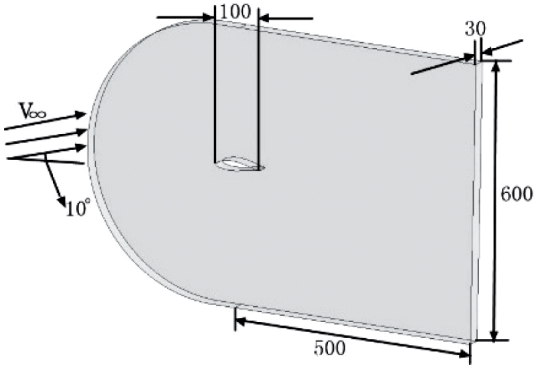

Fig. 1. Computational domain and geometric model of the hydrofoil.

2.1.2. *Calculation model*

In order to ensure the quality of the mesh, the semi-circular area was divided by c-type mesh (as shown in Fig. 2). In order to accurately capture the details of the flow field, the leading and trailing edge regions of the hydrofoil were densified in the region with large edge curvature changes, while the other regions remained sparse. This not only improved the calculation accuracy, but also saved computing resources.

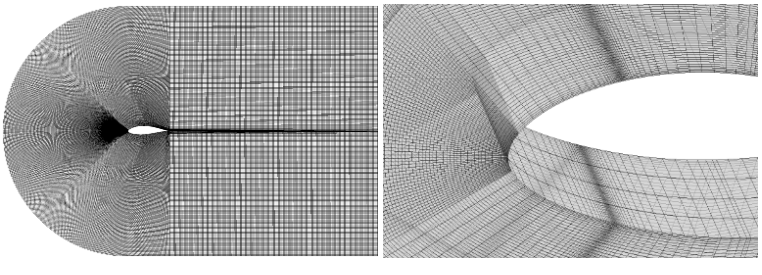

(a) (b)

Fig. 2. Meshing: (a) hydrofoil mesh; (b) local mesh.

In order to eliminate the influence of the number of grids on the accuracy of the numerical calculation, seven sets of grid models with different grid numbers were divided for grid-independent analysis (as shown in Fig. 3). During the process of independence checking of the grid, we found that the static pressure error did not exceed 2.5% as the number of grid cells was more than 1.47 million. These errors were within the allowable range. When the number of grid cells was increased, it had little effect on values of the static pressure. Therefore, the total number of grids in the computational domain were finally determined as approximately 1.47 million, and the minimum grid size was 1.978×10^{-4} mm.

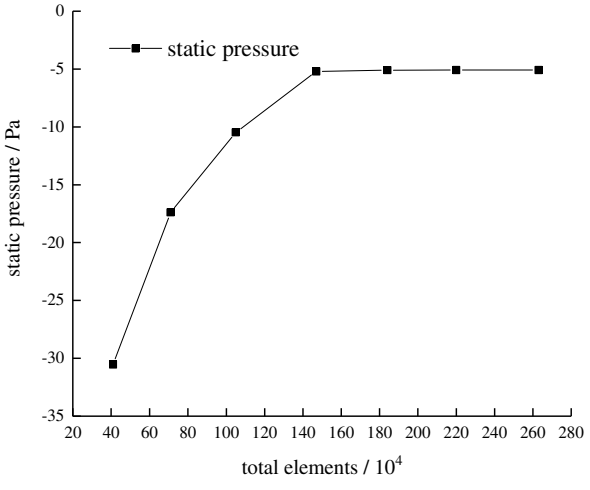

Fig. 3. Grid independence test.

In order to meet the requirements of the LES on the grid mesh of the boundary layer at the wall, the $y+$ distribution of the hydrofoil grid near the wall was examined, as shown in Fig. 4. It can be seen that $y+ < 1$ satisfied the calculation requirements of LES.

Fig. 4. (Color online) Grid wall $y+$ distribution.

In order to investigate the effect of *Re* on hydrofoil acoustic radiation in a certain angle of attack, five different *Re* (*Re* = 10,000–30,000) were analyzed at an angle of attack of 10°. The incompressible liquid water at a temperature of 20°C and a standard atmospheric pressure was defined as the flow medium. The LES viscous model with wall adapting local eddy-viscosity (WALE) sub grid model was used to explore the complicated flow structure.[10] Velocity inlet, outflow outlet, and nonslip wall were set as the boundary condition for the flow field simulation, respectively. Pressure velocity coupling solver adopted the SIMPLE algorithm, and the second-order upwind difference format was used for the calculation. The convergence residual was set as 10^{-6}. According to the Nyquist sampling theorem, the highest frequency of the recoverable sound field was half of the sampling frequency. Assuming that the highest frequency was 2000 Hz, the sampling frequency was 4000 Hz, so the value of the unsteady calculation time step was 2.5×10^{-4} s. Low frequency (≤180 Hz) information with three representational *Re* (10,000; 20,000; and 30,000) were intercepted for acoustic analysis in the paper. The *Re* can be described as Eq. (1).

$$Re = \frac{v_\infty D}{\nu}, \tag{1}$$

where ν is the kinematic viscosity of the fluid, D is the chord length of the hydrofoil, and v_∞ is the inflow velocity; the inflow velocity under different *Re*, as shown in Table 1, are the physical parameters of water at a temperature of 20°C and a standard atmospheric pressure, as shown in Table 2.

Table 1. Reynolds number and inlet velocity.

Working condition	*Re*	v_∞ (m/s)
1	10,000	0.1007
2	15,000	0.1511
3	20,000	0.2014
4	25,000	0.2518
5	30,000	0.3021

Table 2. Physical parameters of water at a temperature of 20°C and a standard atmospheric pressure.

Physical parameter	Unit	Value
Kinematic viscosity	m^2/s	1.007×10^{-6}
Density	g/cm^3	0.998
Acoustic velocity	m/s	1482

2.2. *Sound field numerical calculation method*

2.2.1. *Acoustic calculation method*

At present, Lighthill acoustic analogy theory,[11] Kirchhoff theory,[12] and Powell vortex theory[13] are the three classic theories about fluid dynamic noise. The Lighthill equation can be used to solve the acoustic field caused by hydrodynamic sound by classical acoustic method. This equation is suitable for free space without a boundary. Thus, the Lighthill acoustic analogy theory was selected to analyze the turbulence-induced acoustic characteristics of the hydrofoil in the paper. The Lighthill equation can be expressed as follows[14]:

$$\left(\frac{\partial^2}{\partial t^2 {c_0}^2} - \nabla^2\right)\rho = \nabla \cdot \nabla T_{ij}, \tag{2}$$

where T_{ij} is the stress tensor, described as Eq. (3).

$$T_{ij} = \rho u_i u_j - \tau_{ij} + \delta_{ij}[(P - P_0) - {c_0}^2(\rho - \rho_0)], \tag{3}$$

where $\rho u_i u_j$ is the Reynolds stress caused by the flow velocity, τ_{ij} is viscous stress caused by the fluid viscosity, and $\delta_{ij}[(P - P_0) - {c_0}^2(\rho - \rho_0)]$ is the heat conduction. Among them, δ_{ij} is the Kronecker function: when $i = j$, $\delta_{ij} = 1$; when $i \neq j$, $\delta_{ij} = 0$; ρ is the density of fluid; ρ_0 is the density of fluid when it is not disturbed; u is the velocity; P is the pressure of fluid; P_0 is the pressure of fluid when it is not disturbed; c_0 is the speed of sound; t is the time; i, j is the direction component of the coordinate axis, which complies with the summation agreement in tensor. The Lighthill equation states that the quadrupole sound source of a hydrodynamic sound source is the stress variation in turbulence flow.

Acoustic numerical calculation methods mainly include the finite-element method (FEM), boundary element method (BEM), an acoustic line method, statistical energy method, and acoustic–vibration coupling calculation method. The BEM is separated into the direct boundary element method (DBEM) and the indirect boundary element method (IBEM). Since the BEM is a numerical calculation method based on integral equations, it can convert the volume fraction of the calculation domain into the area fraction on the boundary and reduce the dimension and the number of grids without decreasing the calculation efficiency, which saves computational resources,[15,16] and can be calculated by solving integral equations. The turbulent noise calculation of the three-dimensional hydrofoil was performed using the IBEM module in LMS Virtual lab Acoustics. Therefore, this paper mainly used the IBEM module in LMS Virtual lab Acoustics to calculate the turbulent noise of the three-dimensional hydrofoil.

2.2.2. *Sound field calculation*

The vibration of the hydrofoil was neglected in the simulation. Take the leading edge of the hydrofoil as the coordinate origin B (0, 0, 15), monitoring point A was set at 300 mm from the leading edge of the hydrofoil; monitoring point C was set

at 100 mm; and monitoring point D was set at 400 mm. Four monitoring points (E, F, G, H) were successively set up at 15 mm and 150 mm above and below the mid-point of the hydrofoil. The location of the monitoring points is shown in Fig. 5. After the monitoring data tended towards stability or obvious periodic changes, velocity source items were derived and imported into the Virtual Lab software to calculate the quadrupole noise by the fast Fourier transform with IBEM. The transform was converted into a quadrupole sound source boundary condition, and the sound field was calculated to obtain an acoustic response curve of the monitoring point.

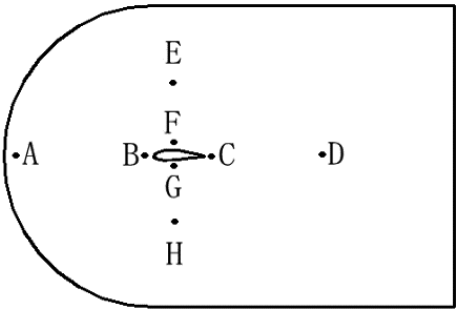

Fig. 5. Monitoring point distribution.

3. Analysis of Numerical Calculation Results of Flow Field

3.1. *Experimental verification of velocity field*

In order to study the turbulence characteristics of a three-dimensional hydrofoil, an experimental study was carried out in a self-circulation high precision variable slope flume. The main components of the experimental system included a self-circulation high precision variable slope flume, water supply equipment, an automatic flow measurement system, an automatic water level measuring instrument, and a three-dimensional acoustic Doppler velocimeter. The flume body had a length of 13 m, both width and depth were 0.6 m, and it had a maximum flow velocity of 0.5 m/s. The flume test mainly controls the flow through the closed-loop control and regulation system, as shown in Fig. 6(a). Figure 6(b) shows the distribution of the average velocity at different positions of x_0/c along the mainstream direction (x), where x_0 is the horizontal distance from the leading edge of the hydrofoil and c is the chord length of the hydrofoil. The height of the distance chord from the sampling point was 15 mm. comparing the flow field data obtained by numerical simulation with the experimental results, it can be concluded that the maximum relative error was 5.8% and the average relative error was less than 5%. The numerical simulation agreed well with the experimental results, which shows the numerical calculation results were credible.

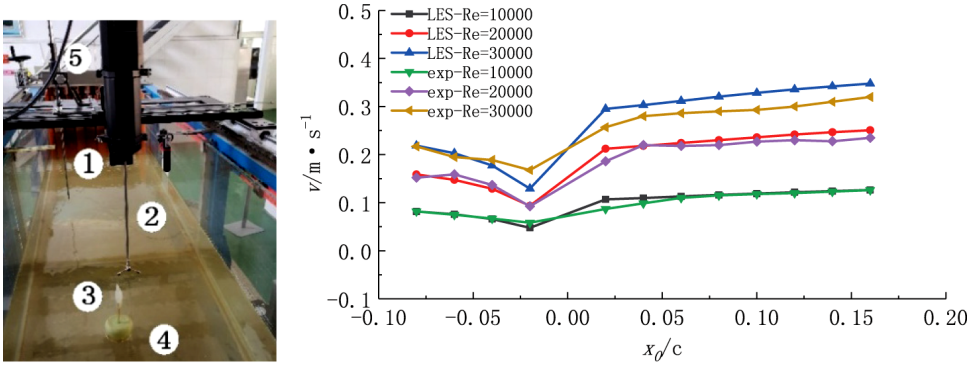

Fig. 6. (Color online) Comparison of experimental values with simulated values: (a) Experimental system; 1: Automatic water level measuring instrument; 2: Three-dimensional acoustic Doppler velocimeter; 3: Hydrofoil; 4: Base and bracket; 5: Self-circulation high precision variable slope flume and (b) average velocity component distribution in the x-direction.

3.2. *Coefficient of lift and drag*

Figure 7 shows the variation of the lift coefficient (C_L) and drag coefficient (C_D) of the hydrofoil during the nonsteady state calculation. It can be seen that the C_L and the C_D of the hydrofoil changed periodically with time, and the fluctuation cycle time of the C_L and the C_D decreased with the increase of the *Re*. It can be deduced that a cyclically varying vortex shedding phenomenon occurred in the flow region and the vortex shedding velocity increased with the increase of the *Re*. Compared with the lift coefficient, the fluctuation of the C_D was more disordered. The principal cause of this phenomenon was that the direction of hydrofoil resistance was consistent with the vortex shedding, and the size and shape of the shedding vortex were irregular.

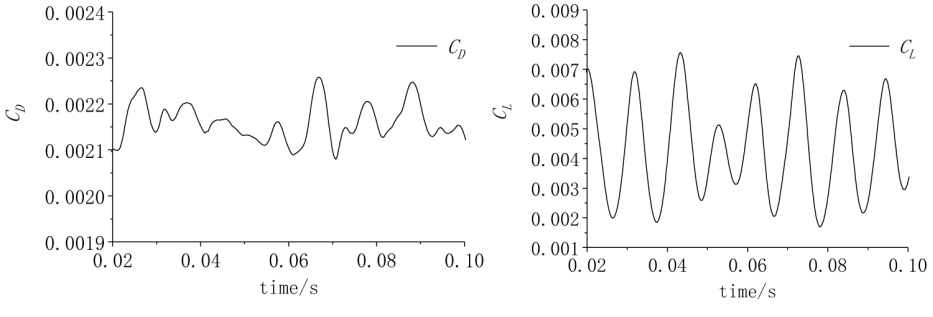

Fig. 7. The fluctuation of lift and drag coefficients: (a) Re = 10,000; (b) Re = 20,000 and (c) Re = 30,000.

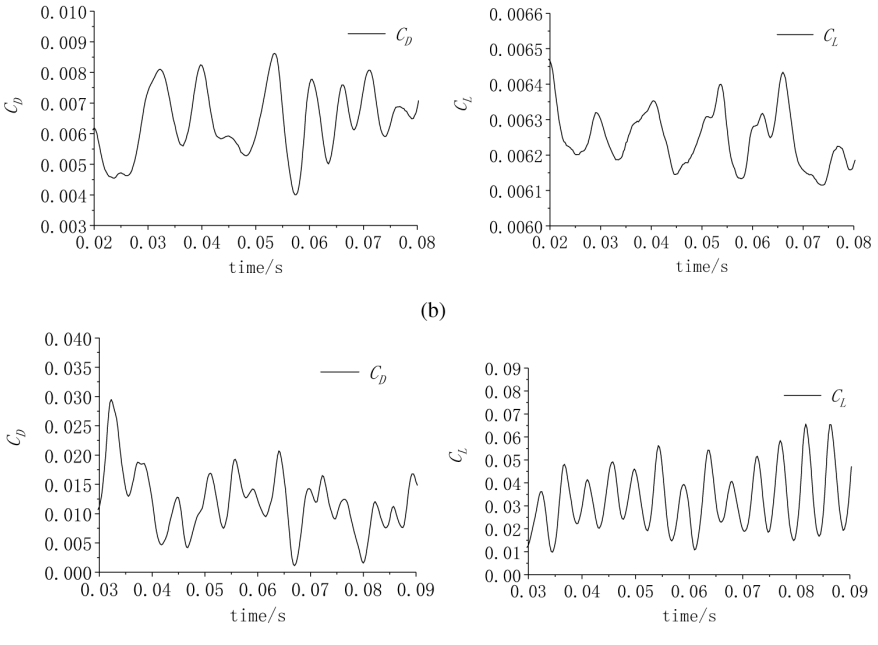

Fig. 7. (*Cont'd*)

3.3. *Analysis of instantaneous flow field*

The transient analysis method was used to study the formation and evolution of the vortex of the hydrofoil with different *Re*.

Figures 8–10 show the instantaneous flow diagram at different moments in the pseudo-period of the hydrofoil vortex shedding with different *Re*. T is a period of complete vortex shedding. The evolution of flow structure at the trailing edge of hydrofoil can be observed through the flow line cross-sectional profile of the hydrofoil surface. In a period of complete vortex shedding, it can be clearly observed that the variation of the upper edge of the airfoil was basically the same. First, a vortex was generated near the upper edge near the tail and gradually moved backward, and finally a new vortex was generated. It was found that the open separation size of the upper edge of the airfoil decreased as the Reynolds number increased.

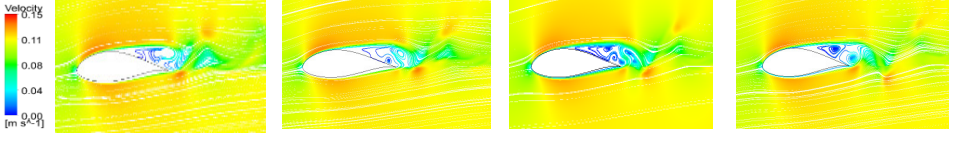

(a) (b) (c) (d)

Fig. 8. (Color online) Streamline diagram as $Re = 10{,}000$: (a) $t_0+T/4$; (b) $t_0+2T/4$; (c) $t_0+3T/4$ and (d) $t_0 + 4T/4$.

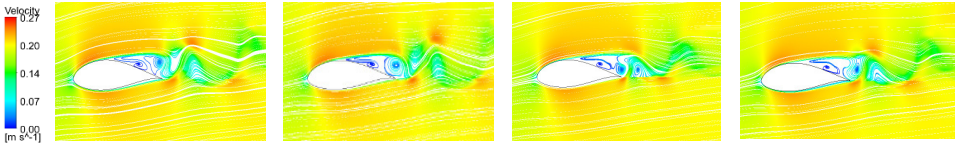

Fig. 9. (Color online) Streamline diagram as $Re = 20{,}000$: (a) $t_0+T/4$; (b) $t_0+2T/4$; (c) $t_0+3T/4$ and (d) $t_0 + 4T/4$.

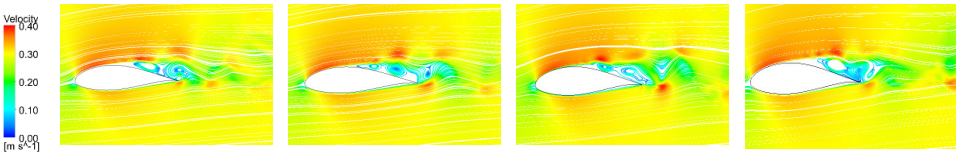

Fig. 10. (Color online) Streamline diagram as $Re = 30{,}000$: (a) $t_0 + T/4$; (b) $t_0 + 2T/4$; (c) $t_0 + 3T/4$ and (d) $t_0 + 4T/4$.

The changes of instantaneous vortex core structure at different moments in a pseudo-period based on the Q criterion were obtained, as shown in Figs. 11–13. It can be observed that the change of the Re affected the distribution of the vortex core. The vortex core was mainly distributed around the hydrofoil, especially at the tail of the hydrofoil. With the increasing Re, the form of the vortex structure changed greatly. Not only the large-scale vortex structure gradually broke into a small-scale vortex structure, but also the position of the initial vortex shedding was gradually approached the leading edge of the hydrofoil.

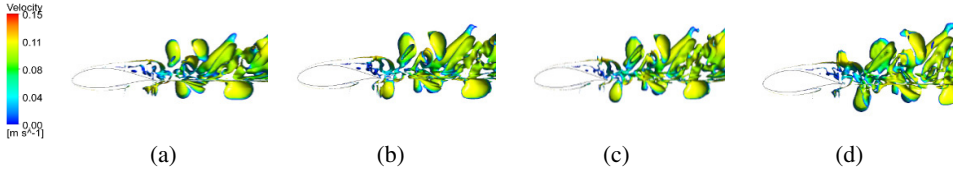

Fig. 11. (Color online) Vortex core structure as $Re = 10{,}000$: (a) $t_0 + T/4$; (b) $t_0 + 2T/4$; (c) $t_0 + 3T/4$ and (d) $t_0 + 4T/4$.

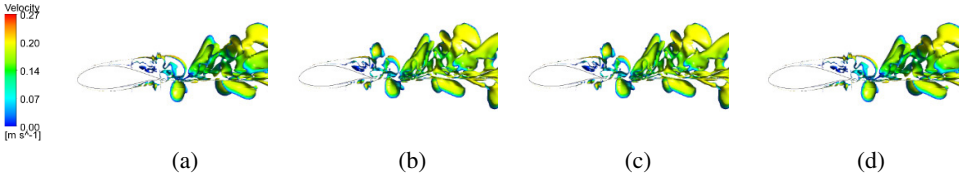

Fig. 12. (Color online) Vortex core structure as $Re = 20{,}000$: (a) $t_0 + T/4$; (b) $t_0 + 2T/4$; (c) $t_0 + 3T/4$ and (d) $t_0 + 4T/4$.

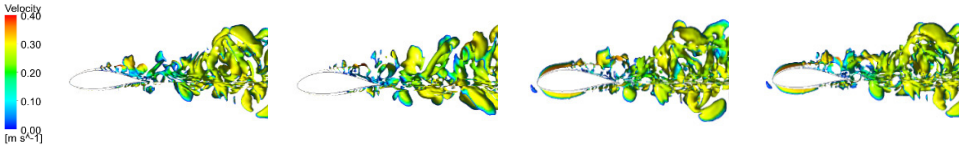

(a) (b) (c) (d)

Fig. 13. (Color online) Vortex core structure as Re = 30,000: (a) $t_0 + T/4$; (b) $t_0 + 2T/4$; (c) $t_0 + 3T/4$ and (d) $t_0 + 4T/4$.

Figures 14–16 are instantaneous velocity curl contours at different moments in the pseudo-period of the hydrofoil vortex shedding under different Re based on the Q criterion. The process of alternate generation, shedding, breaking, and dissipation of the hydrofoil wake vortex could be obviously observed. The vortex near the hydrofoil began to form at the upper half of the hydrofoil and migrated toward the tail until it fell off, broke, and then gradually spread. The velocity curl at the trailing edge of hydrofoil was greater than other parts. The maximum Velocity curl was located at the position of the vortex formation and shedding. As Re increased, the intensity of the vortex increased, and the shedding period decreased.

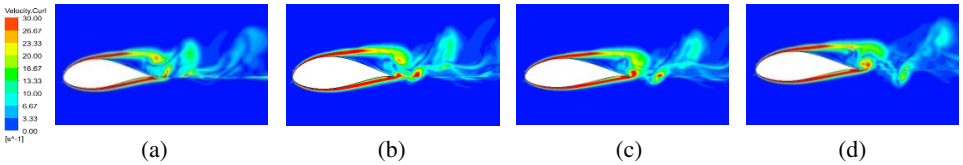

(a) (b) (c) (d)

Fig. 14. (Color online) Velocity curl contours as Re = 10,000: (a) $t_0 + T/4$; (b) $t_0 + 2T/4$; (c) $t_0 + 3T/4$ and (d) $t_0 + 4T/4$.

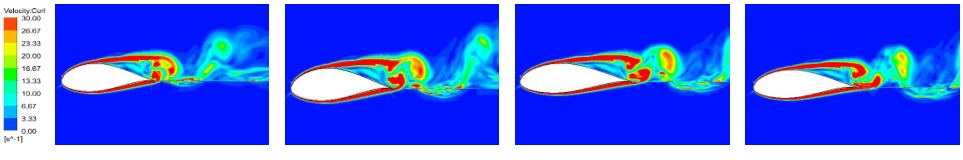

(a) (b) (c) (d)

Fig. 15. (Color online) Velocity curl contours as Re = 20,000: (a) $t_0 + T/4$; (b) $t_0 + 2T/4$; (c) $t_0 + 3T/4$ and (d) $t_0 + 4T/4$.

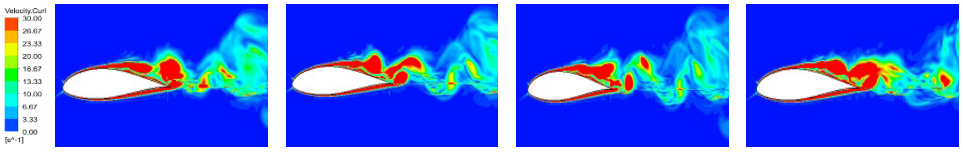

(a) (b) (c) (d)

Fig. 16. (Color online) Velocity curl contours as Re = 30,000: (a) $t_0 + T/4$; (b) $t_0 + 2T/4$; (c) $t_0 + 3T/4$ and (d) $t_0 + 4T/4$.

3.4. *Correlation analysis between vortex characteristic variables and Re*

The relationship of the shedding frequency (f_s), L, and $\Gamma_{\max}$ with the Re at the monitoring point C are shown as Fig. 17, where L is the distance from the vortex initial shedding position to the leading edge of the hydrofoil, and $\Gamma_{\max}$ is the maximum value of the vortex intensity during a vortex shedding period. The vortex shedding frequency and the vortex intensity maximum change were basically the same as the distance from the initial shedding position of the vortex to the leading edge of the hydrofoil. Within a certain range, with the increase of Re, f_s gradually increased and L gradually shortened. The starting position of the vortex shedding was getting closer and closer to the leading edge of the hydrofoil and $\Gamma_{\max}$ gradually increased.

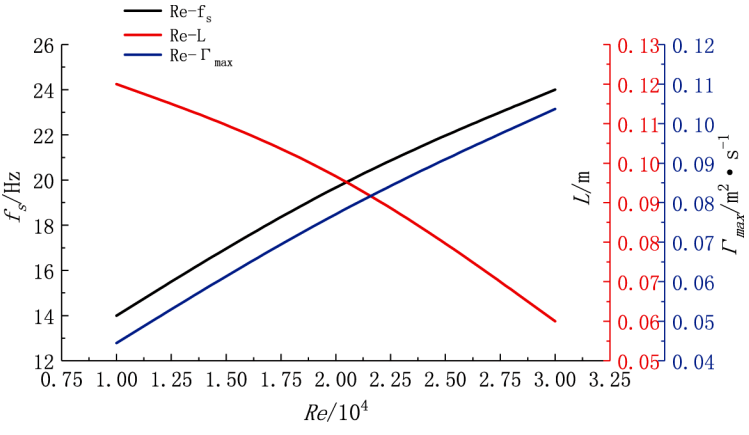

Fig. 17. (Color online) Curve of vortex characteristic variables and Re.

4. Analysis of Sound Field Numerical Calculation Results

The ratio of the effective value of the sound pressure to the reference sound pressure is the SPL in decibels, shown as Eq. (4)

$$L_p = 20 \lg \frac{P}{P_0}, \tag{4}$$

where P is the instantaneous sound pressure; P_0 is the reference sound pressure; in water, $P_0 = 1 \times 10^{-6}$ Pa.

We observed the distribution law of the sound pressure response under various working conditions and summarized the variation law of SPL at each monitoring point. Figure 18 shows the sound pressure response of each monitoring point under different Re. It can be seen the maximum value of SPL increased with the increase of Re, and the fluctuation amplitude also changed, combined with the flow field analysis, which was due to the increase of the Re. The range of the vortex formed

by the tail of the hydrofoil gradually expanded, affecting the SPL of each monitoring point. Under the same *Re*, the SPL of the monitoring point did not show a more obvious characteristic frequency, and the SPL was larger at the low frequency. As the frequency increased, SPL gradually decreased. Monitoring point B was obviously different from other monitoring points and was at the lowest value; SPL was mostly negative, indicating that the instantaneous sound pressure of the SPL was less than the standard sound pressure in the water.

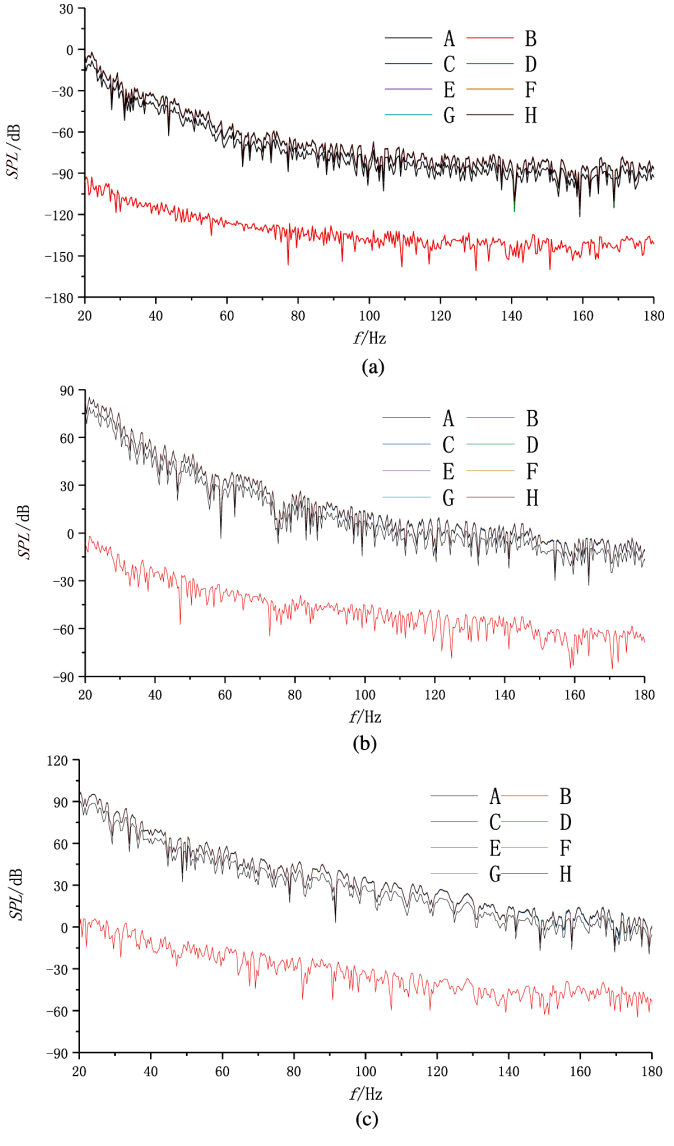

Fig. 18. (Color online) Sound pressure response of monitoring points under different *Re*: (a) *Re* = 10,000; (b) *Re* = 20,000 and (c) *Re* = 30,000.

Figures 19–21 are sound pressure contours with different *Re* at peak frequencies. With the increase of *Re*, the maximum and minimum SPL increased. At the same *Re*, the lower the frequency and the larger the SPL, indicating that the quadrupole noise source was mainly concentrated in the middle and low-frequency bands. The main sound source with high sound pressure was located at the trailing edge and wake of the hydrofoil. This phenomenon was in agreement with the vorticity distribution in the flow field, which showed that the formation, shedding, and diffusion of vortices had an important influence on the scale of the noise SPL.

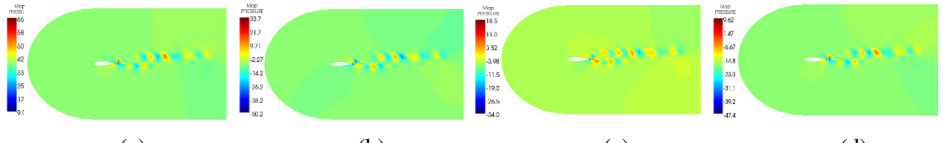

Fig. 19. (Color online) Sound pressure distribution as $Re = 10{,}000$: (a) $f = 20$ Hz; (b) $f = 80$ Hz; (c) $f = 140$ Hz and (d) $f = 180$ Hz.

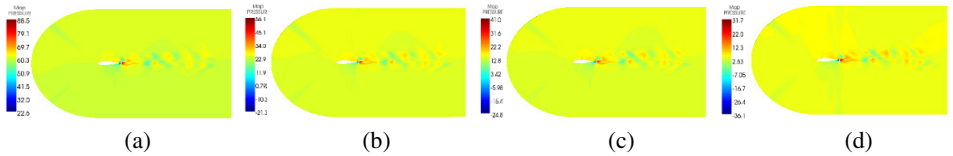

Fig. 20. (Color online) Sound pressure distribution as $Re = 20{,}000$: (a) $f = 20$ Hz; (b) $f = 80$ Hz; (c) $f = 140$ Hz and (d) $f = 180$ Hz.

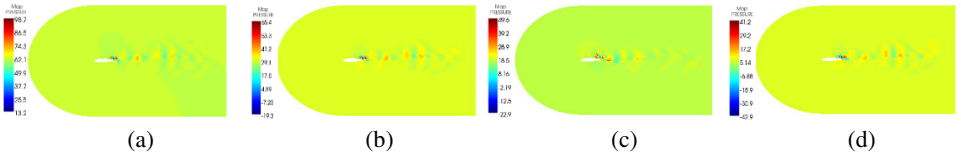

Fig. 21. (Color online) Sound pressure distribution as $Re = 30{,}000$: (a) $f = 20$ Hz; (b) $f = 80$ Hz; (c) $f = 140$ Hz and (d) $f = 180$ Hz.

There were also big differences in the way sound was transmitted at different frequencies. The SPL at point F of the hydrofoil was the largest, which was the smallest at point B. The SPL data of monitoring point F and monitoring point B were extracted, and the changes in the sound pressure response under different *Re* were obtained, as shown in Fig. 22. At the same *Re*, the maximum value of the SPL of monitoring point B was significantly smaller than the maximum SPL of monitoring point F. Monitoring point B and F showed similar change trends under different *Re*. The SPL reached the maximum and minimum when *Re* was 30,000 and 10,000 with the same frequency, respectively. Therefore, the *Re* had a certain influence on the noise.

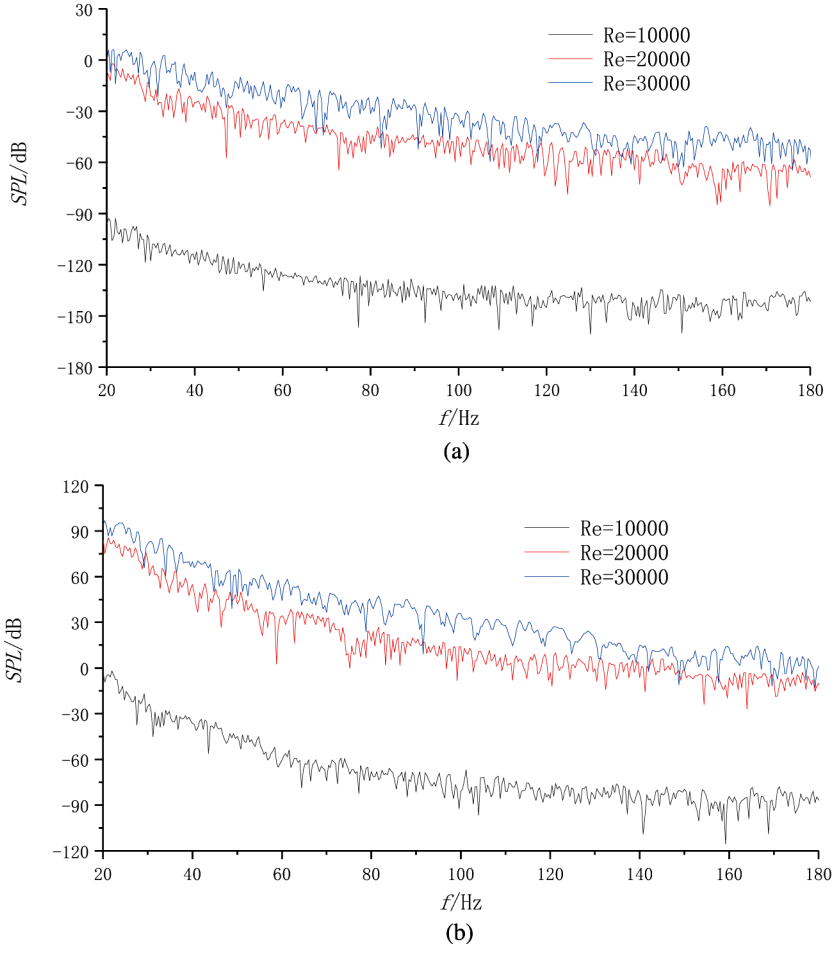

Fig. 22. (Color online) Sound pressure response with different *Re*: (a) Monitoring point B and (b) monitoring point F.

The SPL of the center frequency of each frequency band to the F monitoring point under different *Re* was superimposed to obtain the total sound pressure level (TSPL) of the hydrofoil. Equation (5) is as follows:

$$L_P = 10 \lg \sum_{i=1}^{n} 10^{(0.1 L_{pi})}. \tag{5}$$

In the equation, L_P(dB) represents the TSPL after synthesis; L_{pi}(dB) represents the SPL of different sound sources or different frequency bands. Figure 23 is a characteristic curve of *Re* and TSPL at the monitoring point F. It can be seen from the graph analysis that within a certain range, as the *Re* increases, the TSPL gradually increases and the rate of the increase gradually decreases. Further explanation of the change in *Re* has a certain influence on the turbulent noise of the fluid.

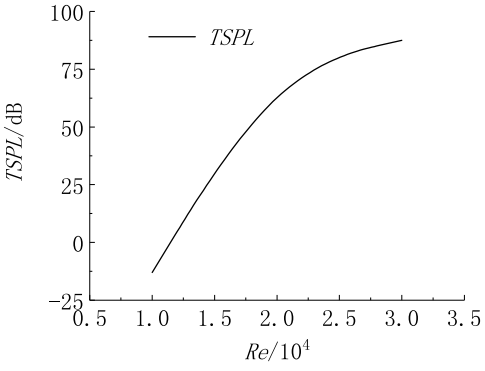

Fig. 23. *Re* and TSPL characteristic curve.

It is known that the ω, $\Gamma_{\max}$, and TSPL of point C under different *Re*. The equations of the fitted equations are obtained by the "polyfit" instruction in matable, and the formulas of the ω and TSPL, $\Gamma_{\max}$, and TSPL are obtained. The TSPL and the $\Gamma_{\max}$ and ω values are both quadratic positively correlated, shown as Eqs. (6) and (7). Figure 24 is the relationship between the TSPL and the vortex characteristic parameters at monitoring point C. It can be seen from the figure that the TSPL increases with the increasing of $\Gamma_{\max}$ and velocity curl (ω), and the increasing rate with $\Gamma_{\max}$ is slightly larger than the increment with ω. In other words, shedding and diffusion of vortices are the critical factors of the generation of the quadrupole source noise.

$$\mathrm{TSPL}(\omega) = -0.0033\omega^2 + 1.4053\omega - 62.4667, \tag{6}$$

$$\mathrm{TSPL}(\Gamma_{\max}) = -34{,}722.8567{\Gamma_{\max}}^2 + 6846.2177\Gamma_{\max} - 249.04067. \tag{7}$$

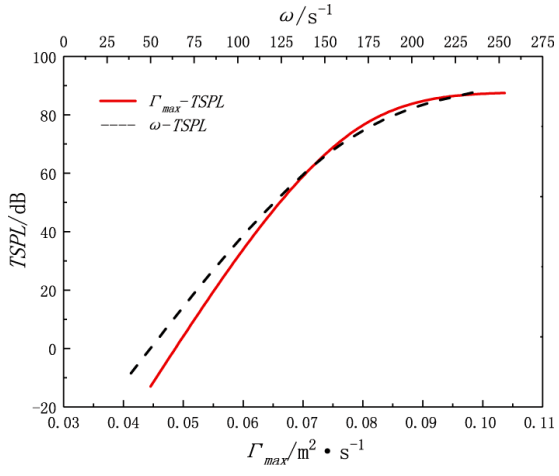

Fig. 24. (Color online) TSPL and vortex characteristic parameter curve.

5. Conclusions

The variation in the flow field and sound field in a turbulent flow around a hydrofoil under different conditions is compared and analyzed. The conclusions are as follows:

(i) The relationship between the flow *Re* and the three-dimensional hydrofoil turbulence is established. The larger the $\Gamma_{\max}$, the shorter the L, and the higher the f_s.

(ii) The relationship between *Re* and SPL of the quadrupole source is constructed. Under different *Re*, the SPL of each monitoring point increases with increases of *Re*. The quadrupole noise has a large impact on the low-frequency band, and the maximum SPL is related to the location of the vortex shedding.

(iii) The relationship between the vortex characteristic parameters and the TSPL is constructed. The main source of the hydrofoil is located in the trailing edge and wake of the hydrofoil. This phenomenon is consistent with the velocity curl distribution of the flow field. The TSPL and the $\Gamma_{\max}$ and ω values are both positively correlated, which shows that the vortex shedding and diffusion are the root cause of the quadrilateral source noise generated by the hydrofoil.

Acknowledgments

This study was supported by the National Key R&D Program Projects of China (Grant No. 2018YFB0606100), the National Natural Science Foundation of China (Grant Nos. 51669012 and 51966010)

References

1. Z. Y. He, *J. Appl. Acoust.* **21** (2002) 26.
2. Q. Zhang, *Pneumatic Acoustic Basis* (National Defense Industry Press, Beijing, 2012).
3. G. D. Fan, Y. Chen and H. X. Hua, *J. Noise Vib. Control* **36** (2015) 56.
4. G. Y. Ai and J. Ye, *J. Acta Aerodyn. Sin.* **35** (2017) 299.
5. S. L. Long, H. Nie and X. Xu, *J. Technical Acoust.* **30** (2011) 111.
6. D. Casalino, M. Jacob and M. Roger, *AIAA J.* **41** (2003) 182.
7. B. Greschner, F. Thiele, D. Casalino *et al.*, *J. Econ. Hist. Rev.* **47** (2013) 310.
8. J. C. Giret, A. Sengissen, S. Moreau *et al.*, Prediction of the sound generated by a rod-airfoil configuration using a compressible unstructured LES solver and a FW-H analogy, in *18th AIAA/CEAS Aeroacoustics Conf.*, Colorado Springs, USA, 4–6 June 2012 (American Institute of Aeronautics and Astronautics, Washington, USA, 2012).
9. J. Boudet, D. Casalino, M. C. Jacob *et al.*, Prediction of broadband noise: Airfoil in the wake of a rod, in *42nd American Institute of Aeronautics and Astronautics Aerospace Sciences Meeting*, Reno, USA, 5–8 January 2004 (American Institute of Aeronautics and Astronautics, Washington, USA, 2004).
10. F. Nicoud and F. Ducros, *J. Flow Turbul. Combust.* **62** (1999) 183.
11. M. J. Lighthill, *J. Proc. R. Soc. Lond. Ser. A: Math. Phys. Sci.* **267** (1962) 147.
12. G. R. Kirchhoff, *J. Ann. Phys.* **254** (2010) 663.

13. M. S. Howe, *Theory of Vortex Sound* (Cambridge University Press, Cambridge, UK, 2003).
14. Q. R. Si, G. C. Sheng, Y. G. Heng *et al.*, *J. Vib. Shock* **37**(23) (2018) 92.
15. D. C. Rodopoulos *et al.*, *J. Eng. Anal. Bound. Elem.* **106** (2019) 160.
16. F. L. Zhan and J. W. Xu, *Virtual.Lab Acoustics Simulation Calculations from Getting Started to Proficient* (Northwestern Polytechnical University Press, Xi'an, China, 2013).